

www.acsami.org Research Article

Electrochemistry at Back-Gated, Ultrathin ZnO Electrodes: Field-Effect Modulation of Heterogeneous Electron Transfer Rate Constants by 30× with Enhanced Gate Capacitance

Yuxin Wang, Yan Wang, and C. Daniel Frisbie*



Cite This: ACS Appl. Mater. Interfaces 2023, 15, 9554–9562



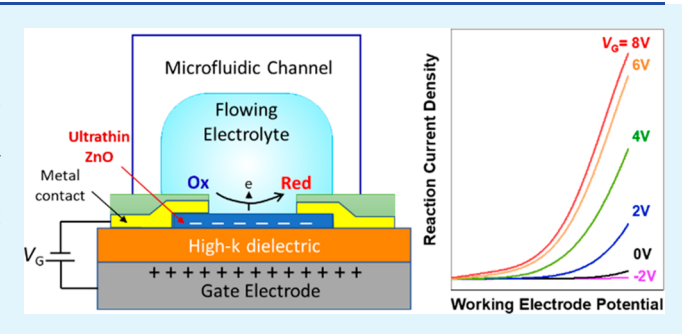
ACCESS I

III Metrics & More

Article Recommendations

Supporting Information

ABSTRACT: We report steady-state voltammetry of outer-sphere redox species at back-gated ultrathin ZnO working electrodes in order to determine electron transfer rate constants $k_{\rm ET}$ as a function of independently controlled gate bias, $V_{\rm G}$. We demonstrate that $k_{\rm ET}$ can be modulated as much as 30-fold by application of $V_{\rm G} \leq 8$ V. The key to this demonstration was integrating the ultrathin (5 nm) ZnO on a high dielectric constant (k) insulator, HfO₂ (30 nm), which was grown on a Pd metal gate. The high-k HfO₂ dramatically decreased the required $V_{\rm G}$ values and increased the gate-induced charge in ZnO compared to previous studies. Importantly, the enhanced gating power of the



 $Pd/HfO_2/ZnO$ stack meant it was possible to observe a nonmonotonic dependence of $k_{\rm ET}$ on $V_{\rm G}$, which reflects the inherent density of redox acceptor states in solution. This work adds to the growing body of literature demonstrating that electrochemical kinetics (i.e., rate constants and overpotentials) at ultrathin working electrodes can be tuned by $V_{\rm G}$, independent of the conventional electrochemical working electrode potential.

KEYWORDS: heterogeneous charge transfer, high-k dielectric, field effect, electrochemical kinetics, semiconductor electrode, voltammogram, atomic layer deposition

■ INTRODUCTION

In recent work, we and others have demonstrated that the kinetics of electrochemical reactions at semiconductor working electrodes can be manipulated reversibly using an independently controlled gate voltage (V_G) . The key idea is that an ultrathin (<5 nm) semiconductor working electrode is incorporated into a metal/insulator/semiconductor (MIS) stack such that application of a gate voltage between the metal and the semiconductor results in simultaneous charge accumulation and band-edge shifts on the front face of the semiconductor exposed to electrolyte. Both the charge accumulation and band-edge shifts modify the rates of electron transfer from the semiconductor to outer-sphere redox couples in the electrolyte.^{2,4-6} These same effects can also modulate the rate of inner-sphere electrocatalytic reactions (e.g., hydrogen evolution) on the semiconductor surface. Importantly, back-side gate control of charge and band edge position is accomplished independent of, and is cumulative with, the normal electrochemical potential control achieved in an electrochemical cell with a reference electrode. That is, the gate voltage V_G can be used to tune electron transfer rates and electrochemical activity independently at a given working electrode potential $V_{\rm W}$.

So far, we have demonstrated these concepts on ultrathin (\leq 5 nm) ZnO and MoS₂ semiconductor working electro-

des. ^{1,2,7} We believe these experiments have utility in understanding fundamentals of electrochemical processes at semi-conductor electrodes and may also prove useful in enhancing the efficiency of critical electrocatalytic reactions, such as hydrogen or oxygen evolution at metal oxides. We note there are clear analogies between our gate-controlled field effect approach and the work of others that employ poled ferroelectric layers underneath thin film working electrodes. ^{17,18}

A key challenge associated with our initial work was that the $V_{\rm G}$ values required to achieve measurable effects were extremely large, up to 100 V. Note that this is not the voltage applied to the frontside semiconductor/electrolyte interface, which would necessarily cause electrochemical breakdown; rather, it is the backside gate potential across the MIS stack required to achieve a few hundred millielectronvolts band edge shift at the semiconductor/electrolyte interface.

Received: October 14, 2022 Accepted: February 2, 2023 Published: February 13, 2023





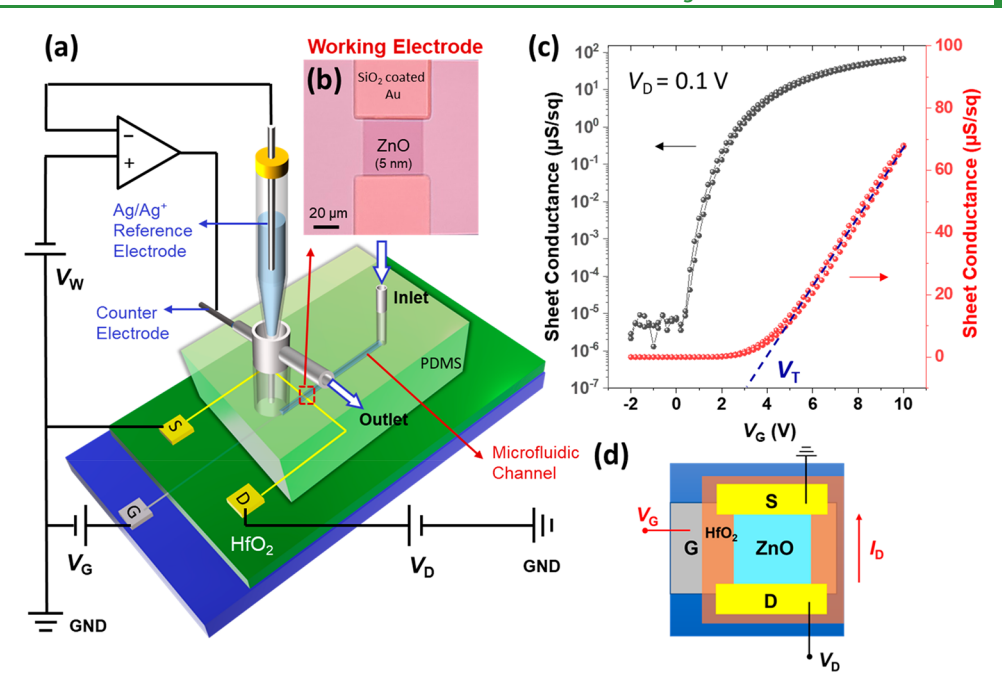


Figure 1. (a) Schematic of the structure and electrical connections of the gate-tunable microfluidic electrochemical cell, with (b) the ultrathin ZnO working electrode. (c) Sheet conductance change of ZnO electrode as a function of V_G , and (d) top view of the device structure.

Such a large voltage is inconvenient, and it is a direct consequence of the low specific capacitance of our previous working electrode MIS stacks. It is well-known that the specific capacitance of a multilayer stack is given by $C = k\varepsilon_0/t$, where k is the dielectric constant of the insulator, ε_0 is the vacuum permittivity, and t is the dielectric thickness. Thus, the low specific capacitance of our previous MIS design reflects both the relatively small dielectric constant ($k \sim 3.8$) of the SiO₂ gate dielectric layer and its large thickness (t = 300 nm). Here, we have switched from 300 nm thick SiO₂ gate insulators to 30 nm thick HfO2 insulator layers. HfO2 is a well-known high-k dielectric material (k ranges from $\overline{15}$ to $\overline{35}$), $\overline{^{19-22}}$ and its increased dielectric polarizability, coupled with a 10-fold decrease in thickness, leads to an over 50-fold increase in the gate capacitance of the MIS stack from 15 nF/cm² for 300 nm SiO_2 to 800 nF/cm² with 30 nm of HfO₂.

The capacitance boost has two positive effects on our experiments that we describe here. First, we are able to achieve strong modulation of heterogeneous electron transfer rates between ZnO and redox couples in solution for gate voltages $V_{\rm G} \leq 8$ V, which is a much more convenient voltage range. Second, we achieve substantially larger changes in heterogeneous electron transfer rate constants $k_{\rm ET}$ than we have obtained previously. This is again a direct consequence of the overall higher gating power accessible with HfO₂. In fact, we show here nonmonotonic dependence of $k_{\rm ET}$ on $V_{\rm G}$ for a simple outer-sphere electron transfer reaction, which we argue reflects the inherent density of redox states in solution and our ability to move the ZnO conduction band edge relative to these states, as will be described.

The new device design is shown in Figure 1. As in our previous work, the patterned 5 nm ZnO film with back-side gate and front-side source/drain contacts is coupled to a microfluidic cell with flowing electrolyte to facilitate steady-state electrochemical measurements (Figure 1a,b). To fabricate the MIS stack, we have employed a Pd gate electrode covered with 30 nm of HfO_2 underneath the ZnO (Figure 1d). As

explained above, the HfO_2 material gives larger gate capacitance. The implications of this are evident in Figure 1c, which displays the ZnO lateral sheet conductance σ_s as a function of V_G between -2 and +10 V. It is clear that strong gate modulation of the in-plane conductance (7 orders of magnitude) is possible with only 10 V. The Figure 1c results will be discussed thoroughly in the Results and Discussion section.

The patterned Pd metal itself also has important advantages, ²³ namely, (1) we are able to grow very uniform, high-quality HfO₂ films on Pd metal by plasma enhanced atomic layer deposition (PEALD) (we were not successful for several other metals like Au), and (2) the Pd dimensions are matched to the ZnO channel dimensions, meaning the gate does not have significant areal overlap with the source and drain leads. This makes the Pd gate less susceptible to shorts and leaks than the large, substrate-sized Si gate we used previously. The Pd/HfO₂ architecture was critical to the success of the whole device structure.

With these design considerations in mind, the main focus of our contribution here is to demonstrate that this new electrode architecture has significant advantages for field effect modulated electrochemistry.

■ EXPERIMENTAL SECTION

Materials Characterization. Thicknesses of atomic layer deposition (ALD)-grown films were measured by ellipsometry (Film-Sense, FS-1, multiwavelength). The thickness was mapped across the wafer for uniformity and fitted with a Cauchy model. The thickness and roughness of the 2D ZnO film were also measured by atomic force microscopy (AFM) (Bruker Instruments Nanoscope V Multimode), with probes from Mikromasch USA (NSC36/Al BS, resonant frequency 65 kHz, k=0.6 N/m, tip radius ~8 nm). The thickness of Pd was measured by a surface profiler (KLA-Tencor P16/P7). The measurement was done with a scan speed of 50 μm/s, sampling rate of 500 Hz, and applied force equal to 2 mg. X-ray photoelectron spectroscopy (XPS) measurements were performed with a PHI Versa Probe III system, using an Al Kα X-ray source. The binding energy was calibrated to the C1s peak at 284.6 eV. X-ray

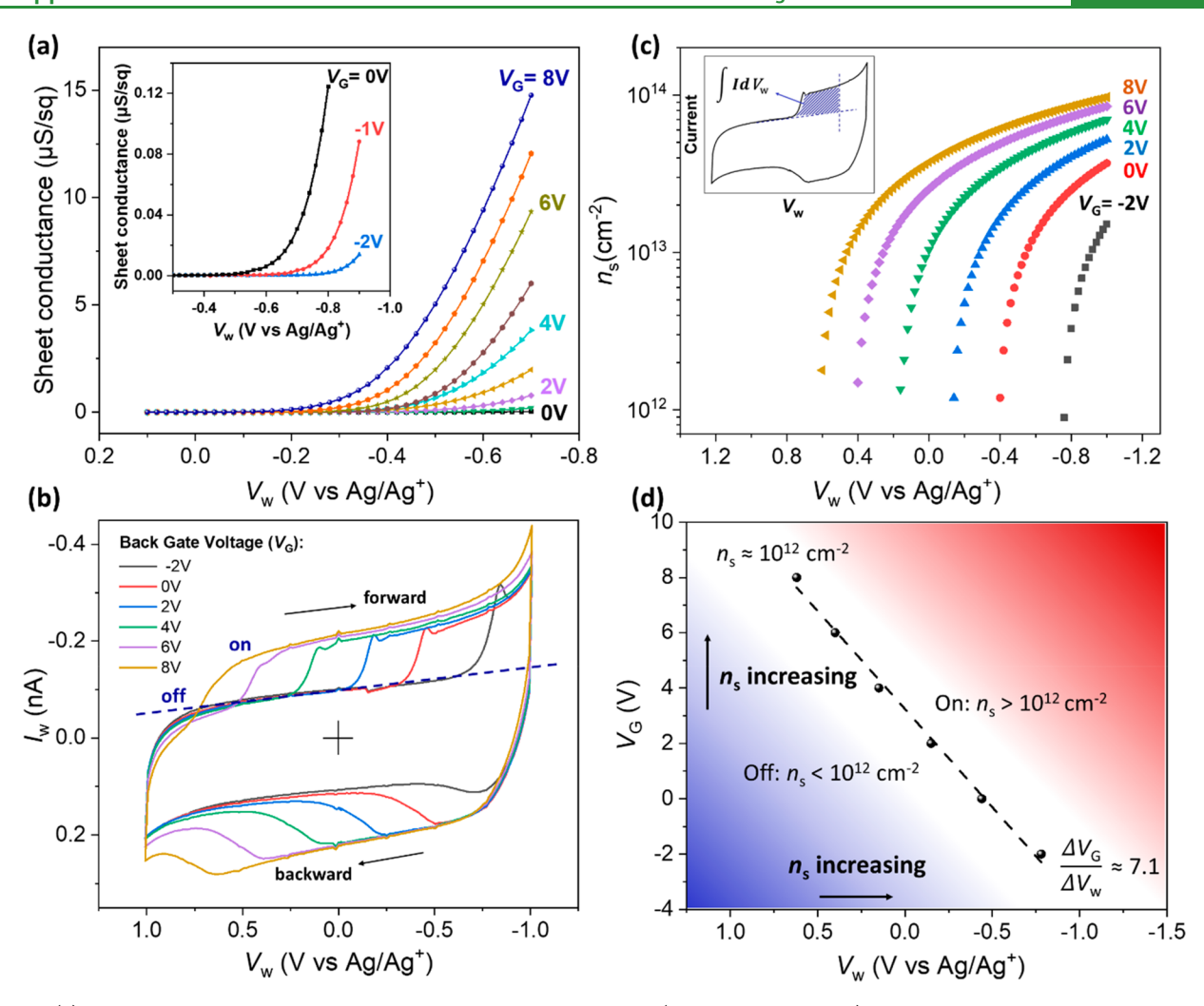


Figure 2. (a) Sheet conductance of the ZnO electrode versus $V_{\rm W}$ in electrolyte (0.1 M TBAP in ACN). The $V_{\rm W}$ sweep rate is 20 mV/s. A drain to source voltage ($V_{\rm D}$) of 5 mV is applied in the measurement. (b) Displacement current ($I_{\rm W}$ vs $V_{\rm W}$) taken in the electrolyte under different back gate voltages ($V_{\rm G}$), with $V_{\rm W}$ sweep rate 420 mV/s. (c) Charge density in ZnO, where the shaded area in the inset figure shows the calculation of total charge injected by $V_{\rm W}$ and $V_{\rm G}$. (d) $V_{\rm G}$ vs $V_{\rm W}$ relationship at a fixed electron density $n_{\rm s} = 2 \times 10^{12}$ cm⁻². Regions of higher (red) and lower (blue) density are indicated.

diffraction (XRD) was measured with a Bruker D8 Discover 2D diffractometer with a Co K α source (λ = 0.179 nm).

Device Fabrication. Figure S6 fully describes the fabrication process of the FET device and the integration of the microfluidic channel. Briefly, 20 nm palladium (Pd) was first deposited on the SiO₂/p-Si substrate by electron beam evaporation (Evaporator CHA, SEC 600) as the gate electrode. The substrate was prepatterned using photolithography, so a local-gate structure was achieved after lift-off. The smaller areas of local gates can help reduce leakage current when applying a gate voltage and prevent the device from breaking down. Next, 30 nm HfO2 was grown by plasma-enhanced ALD (PEALD) (Fiji G2) as the dielectric. The PEALD process involves 230 cycles at 150 °C with alternating pulses of tetrakis(dimethylamido)hafnium (TDMAH, 250 ms) and $\rm O_2$ plasma (300 W, 6 s), with $\rm N_2$ purge in between. ZnO was then deposited right after the deposition of HfO₂ to eliminate possible contamination of the interface. Five nanometers of ZnO was deposited by ALD (Kurt J Lesker) at 200 °C for 50 cycles, pulsing precursors diethylzinc (DEZ) (20 ms) and H₂O (20 ms). Next, ZnO was patterned and etched by wet-etching, and HfO2 was etched by plasma etching (Oxford Etcher, 180-ICP) using 20:5 sccm of BCl₃/Ar, RF power 100 W, 2 mTorr, for 15 s. Then, 5/30/5 nm of Ti/Au/Ti was deposited by electron beam evaporation, followed by a deposition of 70 nm SiO2 to passivate the Au top electrode. After fabrication of the FET, a PDMS microfluidic channel was fabricated and bonded onto the device. The flow channel has a

width of 200 μ m and a height of 50 μ m. The detailed process for building the PDMS channel was reported in prior work.²

Electrochemical Measurement. The instrument setup for electrochemical measurement is illustrated in Figure 1a. The electrolyte used in this study is 0.1 M tetrabutylammonium hexafluorophosphate (TBAP) in acetonitrile (ACN). All solutions were purged with N₂ for 30 min before measurement. The threeelectrode system here consists of the Ag/Ag+ reference electrode (RE) for nonaqueous solution, platinum (Pt) wire counter electrode (CE, d = 0.5 mm), and 2D ZnO as the working electrode (WE). The RE was placed in a Luggin capillary filled with electrolyte, with the tip of the capillary inserted into the flow channel from the outlet side, to minimize potential drop between RE and WE. The device has an inlet where a syringe pump pumps solution into the channel; flow occurs across the working electrode to the outlet. This setup allows for the measurement under controlled flow rates. The electronic measurements, including the transfer performance, displacement current measurement, and the steady-state current measurements were performed with a series of Keithley source meters on a probe station. The detailed models and connections can be found in our previous report.1

RESULTS AND DISCUSSION

We begin this section with a discussion of the field effect conductance results for gated ZnO shown in Figure 1c and then move to electrochemistry.

Field Effect Modulation of the ZnO Sheet Conductance, $σ_s$. The Pd(20 nm)/HfO₂(30 nm)/ZnO(5 nm) stack with front-side Au source and drain contacts on the ZnO constitutes a field effect transistor (FET) architecture. Note that the thickness, surface morphology, and chemical composition of the ZnO, HfO₂, and Pd films were characterized as shown in Figures S1–S5. Uniform thin films of ZnO and HfO₂ can be grown with small roughness and accurate thickness control, and XPS (Figure S2a) confirms the composition. ^{24,25}

The FET architecture can be used to probe the ZnO sheet conductance (σ_s) as a function of V_G and to establish that good field effect control is operative. Inspection of Figure 1c demonstrates that the ZnO sheet exhibits n-channel conduction (as opposed to p-channel conduction) as the device turns ON when $V_{\rm G}$ sweeps positive. We conclude electrons are accumulated in response to the back gate field. Importantly, the ON-to-OFF σ_s ratio is nearly 10⁷, an excellent value reflecting a strong field effect, and the threshold voltage $V_{\rm T}$ (defined on the linear plot) is ~3 V, much lower than we reported previously with the SiO₂-based MIS stack. The low $V_{\rm T}$ value and the absence of significant hysteresis in $\sigma_{\rm s}$ on forward and reverse V_G sweeps indicates that there is minimal electron trapping in the ZnO film. The field effect electron mobility (μ_e) is estimated to be ~14 cm² V⁻¹ s⁻¹, a good value, which is extracted from the slope $(d\sigma_s/dV_G)$ of the sheet conductance $-V_G$ trace according to,

$$\mu_{\rm e} = \frac{\mathrm{d}I_{\rm D}}{\mathrm{d}V_{\rm G}} \times \frac{L}{WV_{\rm D}C_{\rm G}} = \frac{\mathrm{d}\sigma_{\rm s}}{\mathrm{d}V_{\rm G}} \times \frac{1}{C_{\rm G}} \tag{1}$$

where L and W are length and width of the channel, $I_{\rm D}$ is the source-to-drain current, $V_{\rm D}$ is the source to drain bias (100 mV), $\sigma_{\rm s}$ is the sheet conductance of the ZnO channel, and $C_{\rm G}$ is the specific capacitance of the MIS stack.²⁶

To measure C_G , we recorded gate displacement currents^{27,28} (I_G , capacitive charging currents) of the Pd/HfO₂/ZnO stack in response to V_G sweeps. From I_G vs V_G sweep rate plots (Figure S8 in the Supporting Information), we extract $C_G = 800 \text{ nF/cm}^2$, over 50 times higher than our previously used MIS stack.^{1,4} The dielectric constant of the HfO₂ film was calculated to be ~27, which is consistent with the reported values 20

Charge Accumulation in ZnO as a Function of $V_{\rm G}$ and V_{W} . Contacting the ZnO side of the MIS stack with electrolyte in the microfluidic cell shown in Figure 1a allows for two-sided gating of the ZnO film. The carrier density in the ZnO is a function of both the back gate potential $V_{\rm G}$ and the electrochemical potential $V_{\rm W}$ (Figure 1a). This can be assessed in two different ways. Figure 2a displays the ZnO sheet conductance versus $V_{\rm W}$ for different $V_{\rm G}$ values. $\sigma_{\rm s}$ increases as V_W becomes more negative, consistent with double layer charging and electron accumulation in the ZnO working electrode. For a fixed $V_{\rm W}$ value, $\sigma_{\rm s}$ also increases as $V_{\rm G}$ becomes more positive, as expected for normal capacitive charging (Note that the sign conventions for V_G and V_W are opposite to each other such that $V_{\rm G} > 0$ and $V_{\rm W} < 0$ both correspond to electron accumulation in ZnO). Clearly, σ_s is a function of both $V_{\rm G}$ and $V_{\rm W}$, which means that the accumulated electron

sheet density in ZnO can be controlled by voltages on either side of the film. Stated another way, the dielectric and double layer capacitors on either side of the ZnO film are coupled in series.

A similar conclusion can be made from Figure 2b, which displays the electrochemical double layer charging current (I_W) for back-gated ZnO in contact with electrolyte as a function of $V_{\rm W}$ and $V_{\rm G}$. As $V_{\rm W}$ sweeps negative (forward sweep), $I_{\rm W}$ makes a sharp jump to a higher (more negative) value when the ZnO channel opens, i.e., when it floods with electrons.²⁷ On the reverse (discharging) sweep, I_W steps to a lower (less positive) value at approximately the same V_{W} value. V_{W} potentials that are positive of the step correspond to electron depletion in ZnO; potentials negative of the step are in the electron accumulation regime. The step in $I_{\rm W}$ represents the device threshold, the point at which the ZnO conduction band edge has approximately aligned with the Fermi level of the source and drain contacts, allowing electrons to flood the film. It is clear from Figure 2b that the step position depends on V_G ; the more positive V_G is, the more positive V_W becomes at the step. This is anticipated because the electric field resulting from positive V_G values pulls the ZnO conduction band edge down in energy (the field effect), decreasing the negative electrochemical potential $V_{\rm W}$ necessary to reach the threshold.^{29,30} Thus, the threshold for electron accumulation is systematically dependent on both $V_{\rm G}$ and $V_{\rm W}$.

Importantly, the I_W – V_W plots in Figure 2b can be integrated to determine the accumulated electron density in ZnO according to eq 2:²⁷

$$n_{\rm s} = \frac{Q}{eA} = \frac{\int (I_{\rm W,ON} - I_{\rm W,OFF}) dV_{\rm w}}{\frac{dv_{\rm w}}{dt} eA}$$
(2)

where n_s is the electron number density in the ZnO, Q is the total charge, $I_{\rm W,ON}-I_{\rm W,OFF}$ is the charging current measured on the ZnO electrode, where $I_{\rm W,OFF}$ (the OFF-state current) is the baseline, $\int (I_{\rm W,ON}-I_{\rm W,OFF}){\rm d}V_{\rm W}$ corresponds to the shaded area in the inset to Figure 2c, dV_W/dt is the V_W sweep rate, e is the electron charge, and A is the exposed area of ZnO electrode. The resulting electron density n_s is plotted in Figure 2c as a function of V_W and V_G . Notably, the electron density in ZnO can reach the very large value of $10^{14}\ cm^{-2}$ by this double-gating approach at $V_{\rm G}$ = +8 V (vs ground) and $V_{\rm W}$ = $-1~V~vs~Ag/Ag^+$. In our previous experiments we achieved only $5\times 10^{12}~cm^{-2}$. This shows the large tunability of electron occupation in ZnO that can be achieved using a high-k MIS stack and double layer charging in tandem. Additionally, we will use the n_s data in Figure 2b in a later section to extract electron transfer rate constants $k_{\rm ET}$ from electrochemical reaction rates.

To visualize the systematic relationship between $V_{\rm G}$, $V_{\rm W}$, and carrier density in ZnO, we plot $V_{\rm G}$ vs $V_{\rm W}$ at fixed $n_{\rm s}=2\times 10^{12}$ cm⁻² (where the ZnO channel fully opens) (Figure 2d). This graph is illuminating in several ways. First, the clear straightline relationship in Figure 2d means that the two seriescoupled capacitors $C_{\rm G}$ and $C_{\rm W}$ (the double layer capacitor) are behaving ideally, that is, their capacitances are fixed and do not vary with voltage. This conclusion follows by noting that a charge balance on ZnO predicts that at fixed $n_{\rm s}$, $C_{\rm G}\Delta V_{\rm G}=C_{\rm W}\Delta V_{\rm W}$, and thus the slope of the $V_{\rm G}-V_{\rm W}$ plot is $\Delta V_{\rm G}/\Delta V_{\rm W}=C_{\rm W}/C_{\rm G}$, which is also a fixed value if the capacitances are fixed. Thus, from the extracted slope of 7.1 in Figure 2d and the previously determined $C_{\rm G}$ value of 800 nF/cm² = 0.8 μ F/cm²,

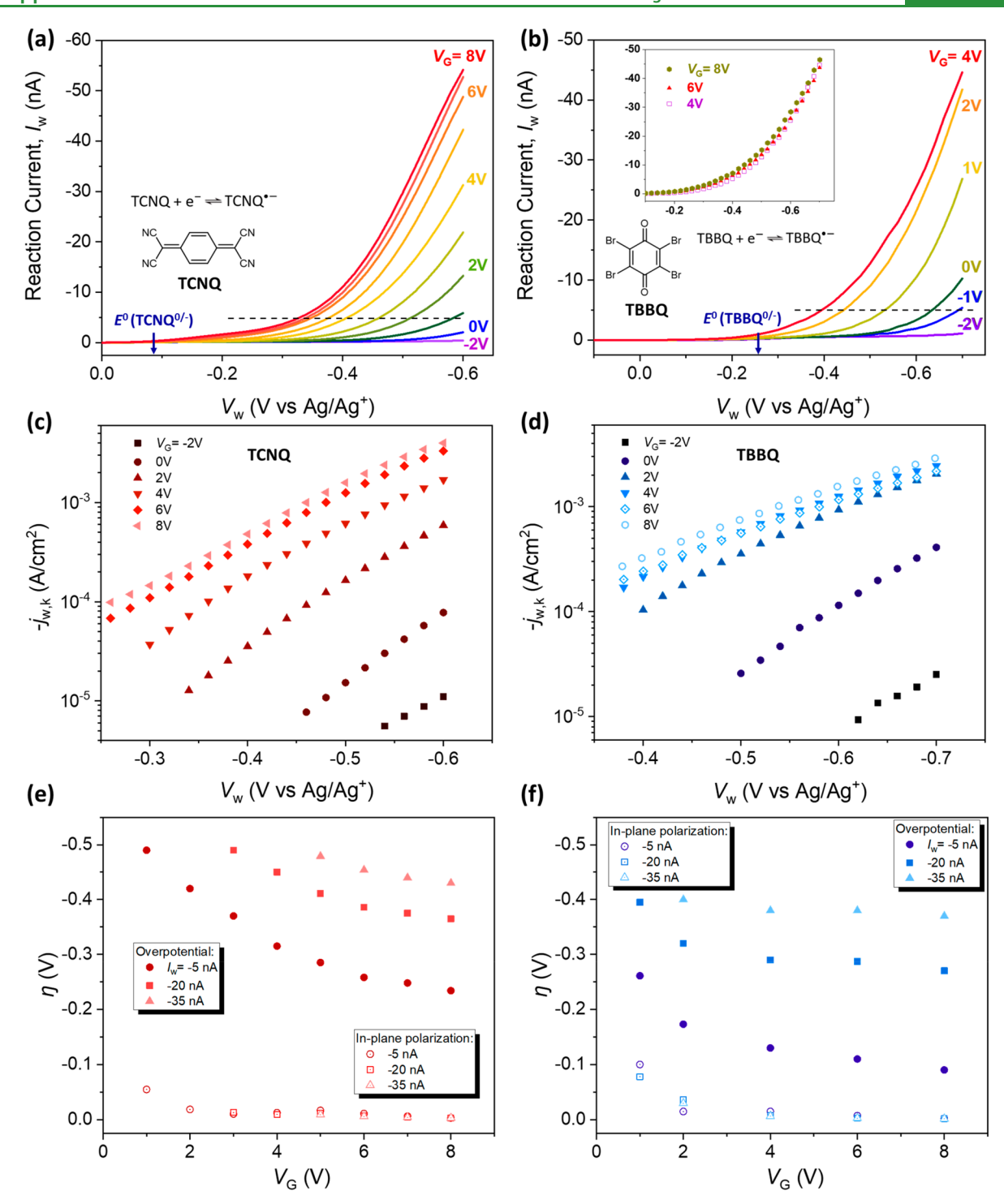


Figure 3. Steady state voltammograms at ZnO under different gate voltages (V_G) for (a) 0.5 mM TCNQ and (b) 0.5 mM TBBQ in 0.1 M TBAP/ACN, respectively, with the flow rate at 10 μ L/min. The V_W sweep rate is 20 mV/s. (c and d) Mass transport corrected reaction current density ($j_{w,k}$) vs V_W under different V_G for 0.5 mM TCNQ and 0.5 mM TBBQ, respectively. (e and f) Overpotential (η) (filled symbols) and in-plane polarization (open symbols) at different V_G and I_W values for TCNQ and TBBQ voltammetry, respectively.

we determine $C_{\rm W}=6\,\mu{\rm F/cm^2}$, which is reasonable for a double layer capacitor. From this, we also see that, while the double layer capacitance $C_{\rm W}$ is indeed dominant, that the back gate capacitance $C_{\rm G}$ is of comparable magnitude ($\sim 1\,\mu{\rm F/cm^2}$).

Steady-State Voltammetry of Redox Couples As a Function of V_G , V_W . Steady-state voltammetry at gated ZnO was carried out in the microfluidic cell shown in Figure 1a with two well-known redox molecules, TCNQ and TBBQ,

separately.^{31–35} These redox species were chosen because of the proximity of their formal potentials (U^0 (TCNQ^{0/–}) = $-0.09 \text{ V vs Ag/Ag}^+$ and U^0 (TBBQ^{0/–}) = $-0.28 \text{ V vs Ag/Ag}^+$)) to the estimated conduction band edge potential for ZnO. Further, their difference in U^0 values turns out to be important to the observed kinetics, as we will see.

Prior to performing voltammetry at ZnO, we established steady-state conditions for the Figure 1a setup using Au band

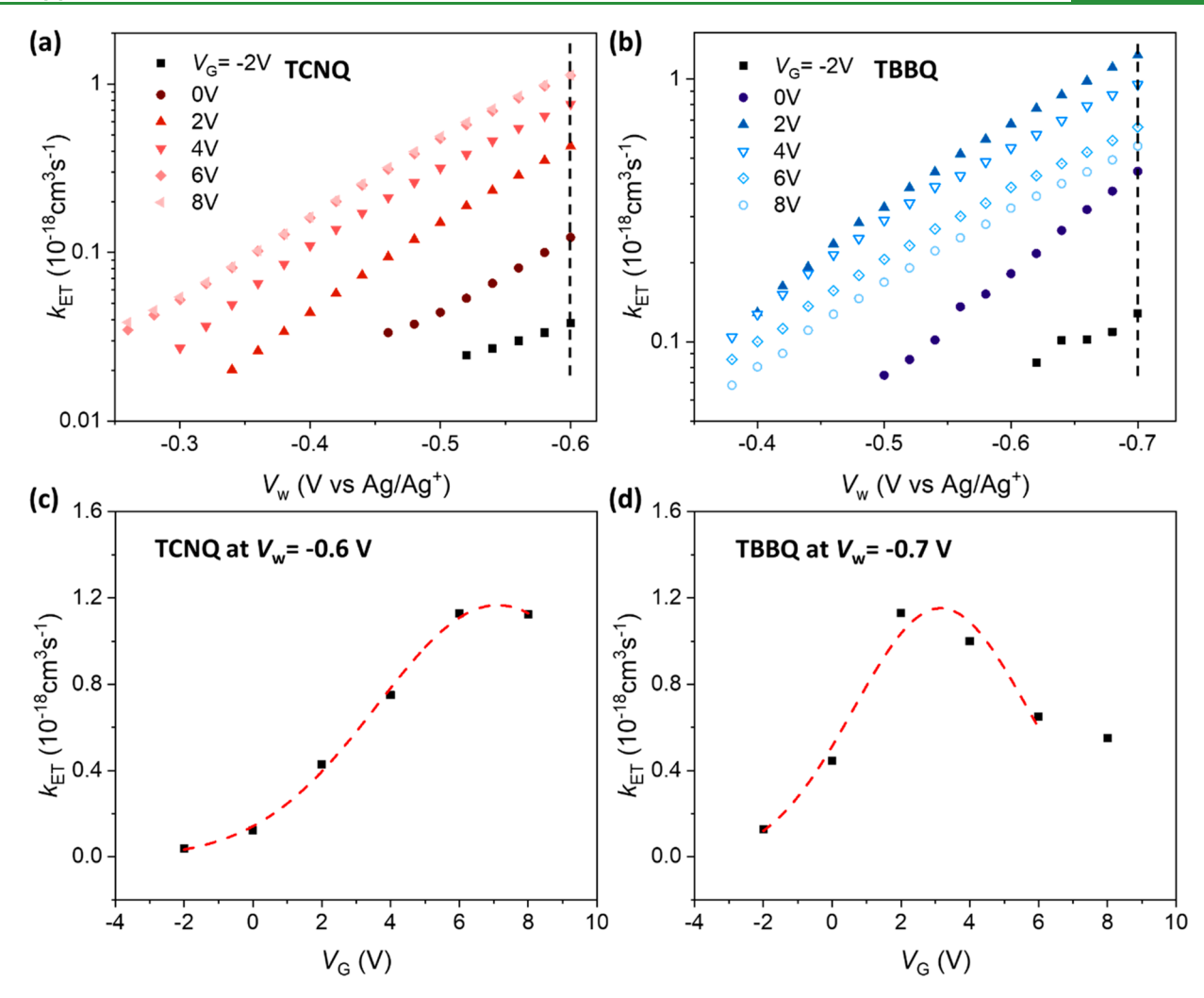


Figure 4. Charge transfer rate constant ($k_{\rm ET}$) plotted vs $V_{\rm W}$ at different $V_{\rm G}$ values for (a) TCNQ and (b) TBBQ voltammetry, calculated from the data in Figure 3. (c and d) Plot of $k_{\rm ET}$ vs $V_{\rm G}$ at $V_{\rm W} = -0.6$ and -0.7 V vs Ag/Ag⁺, respectively, for TCNQ and TBBQ (see vertical dashed lines in a,b).

working electrodes (see Figure S10), as we have reported previously. 4,36

The steady state voltammograms at ZnO for 0.5 mM TCNQ and TBBQ in flowing electrolyte (0.1 M TBAP/ACN, 10 μ L/ min) are shown in Figure 3a,b, respectively. Figure S9 in the Supporting Information displays the corresponding forward and reverse sweeps. It is clear in both Figure 3a and b that the reaction current $I_{\rm W}$ is strongly dependent on $V_{\rm W}$, which means the reduction processes are both limited by reaction kinetics and mass transport. The plateauing of I_{W_t} indicative of the fully mass transport limited regime, is not observed. 36,37 Further, a significant overpotential is required to achieve appreciable reaction rates, which is to be expected for electron transfer at a semiconductor electrode where the formal potentials of the redox species are above the Fermi level $E_{\rm F}$ of the semiconductor. 38,39 It is also evident that there is a strong $V_{\rm G}$ dependence on I_W for both reduction reactions. Generally speaking, positive values of $V_{\rm G}$ strongly increase the reaction current at a fixed V_{W} value. This trend weakens at the highest $V_{\rm G}$ values where increases in $I_{\rm W}$ get progressively smaller with increments in V_G . The V_G dependence will be discussed below.

The reaction current can be corrected for mass transport effects following the Koutecký–Levich equation: ^{36,40}

$$j_{w,k} = \left(\frac{1}{j_w} - \frac{1}{j_{w,\lim}}\right)^{-1} \tag{3}$$

where $j_{\rm w,k}$ is the reaction current density without mass-transport effects, $j_{\rm w}$ is the current density actually measured on the ZnO electrode, $j_{\rm w,lim}$ is the fully mass transport limited current density, which we measured on Au band electrodes. The $j_{\rm w,k}$ values are plotted in Figure 3c,d on a semilog scale. It is striking that $j_{\rm w,k}$ for either TCNQ or TBBQ reduction at $V_{\rm w} = -0.6~{\rm V~vs~Ag/Ag^+}$ can be modulated by well over 2 orders of magnitude by varying $V_{\rm G}$ between -2 and $+8~{\rm V.}$ The $j_{\rm w,k}$ values also increase approximately exponentially with $V_{\rm W}$, as expected.

We can also assess the effect of $V_{\rm G}$ by examining the electrode overpotential $\eta=V_{\rm W}-U^0$ necessary to achieve specific $I_{\rm W}$ values. Figure 3c plots η vs $V_{\rm G}$ at $I_{\rm W}=5$, 20, and 35 nA (the black dashed lines in Figure 3a,b correspond to $I_{\rm W}=5$ nA). One can see that η at $I_{\rm W}=5$ nA decreases by ~250 mV for TCNQ reduction (Figure 3e) and by ~150 mV for TBBQ (Figure 3f) over the full $V_{\rm G}$ range. Thus, significant changes in η are possible by applying a back gate voltage. Critically, we have also overlaid the in-plane polarizations on Figure 3e,f plots. By "in-plane polarization", we mean the potential due to ohmic drop in the ZnO film. One can see that for $V_{\rm G}>2$ V in-

plane polarization is substantially smaller than η , meaning the changes in η reflect real changes in electrode kinetics, not just resistive losses in the ZnO films due to lateral in-plane electron transport.

Electron Transfer Rates As a Function of V_G , V_W . Moving to kinetics, we extract the charge transfer rate constants $k_{\rm ET}$ using eq 4,⁴⁰

$$j_{w,k} = k_{ET} e n_s C_{ox}^* \tag{4}$$

which relates the reaction current density $j_{\rm w,k}$ to $k_{\rm ET}$, the accumulated electron density in the ZnO electrode n_s , and the bulk concentration of reactants C_{ox}^* (TCNQ or TBBQ) in the electrolyte (e is the electron charge). Note that this equation assumes $j_{w,k}$ only reflects reduction current and no anodic current, which is reasonable because $C_{ox}/C_{red} \gg 1$ in our system. From Figure 2, we have n_s as a function of both V_G and $V_{\rm W}$. With $n_{\rm s}$ in hand and $C_{\rm ox}^*$ known from the experimental conditions, we have calculated $k_{\rm ET}$ using eq 4 for both TCNQ and TBBQ reduction reactions, respectively (Figure 4a,b). Inspection shows that $k_{\rm ET}$ is a strong function of both $V_{\rm G}$ and V_{W} . The dependence on working electrode potential V_{W} is expected, but the dependence on $V_{\rm G}$ both confirms our prior report and shows that we can achieve up to a 30× increase in $k_{\rm ET}$ (Figure 4a), far surpassing our previous results. ^{1,4} We will return to this point shortly.

To clarify the influence of $V_{\rm G}$, we have plotted $k_{\rm ET}$ vs $V_{\rm G}$ at fixed values of $V_{\rm W}=-0.6$ and -0.7 V for TCNQ and TBBQ reduction in Figure 4c,d, respectively (see vertical dashed lines in Figure 4a,b). In Figure 4c, we observe an essentially monotonic dependence of $k_{\rm ET}$ on $V_{\rm G}$ with $k_{\rm ET}$ increasing by $\sim 30\times$ from $V_{\rm G}=-2$ to +8 V. For TBBQ on the other hand, the $k_{\rm ET}$ vs $V_{\rm G}$ relationship has a distinct maximum. $k_{\rm ET}$ peaks at about $V_{\rm G}=+3$ V and then decreases with further increases in $V_{\rm G}$.

The striking difference in the $k_{\rm ET}$ vs $V_{\rm G}$ behavior for TCNQ and TBBQ reductions can be explained by the Gerischer model describing charge transfer between semiconductor electrodes and outer-sphere redox couples. Figure 5

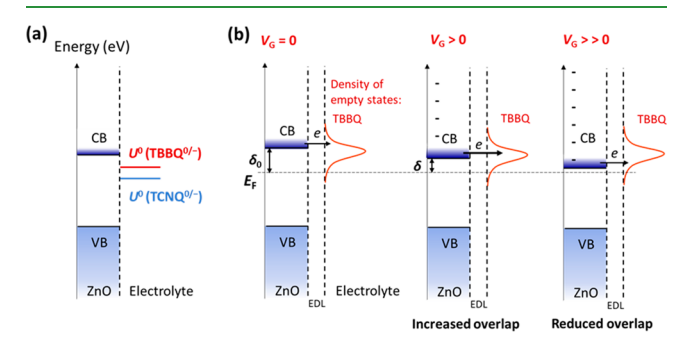


Figure 5. (a) Energy diagram showing the formal potentials (U^0) of TBBQ $^{0/-}$ and TCNQ $^{0/-}$ relative to the ZnO energy levels. (b) Charge transfer process between ZnO electrode and the TBBQ LUMO at $V_{\rm G}=0$ V and $V_{\rm G}>0$. $E_{\rm F}$ is the Fermi level of ZnO, and δ_0 is the initial conduction band (CB) offset from $E_{\rm F}$.

shows a schematic of the heterogeneous charge transfer process in terms of electrode energy bands and the empty density of states for redox acceptor species in solution. We assume that band bending in the 5 nm ZnO film is negligible. In Figure 5b, δ_0 is the initial offset of the conduction band edge from the Fermi level $(E_{\rm F})$. When a positive gate bias $(V_{\rm G}>0)$

is applied, the conduction band edge decreases with respect to $E_{\rm F}$ due to the field effect and electrons accumulate in the band. Here, δ represents the new offset at $V_{\rm G}>0$ where $\delta<\delta_0$. In previous work we have shown that the band edge shift $\Delta\delta=\delta_0-\delta$ can be determined from the following relationship, assuming there are no in-gap traps states near $E_{\rm F}$:

$$\left(\frac{\partial \delta}{\partial V_{\rm G}}\right)_{V_{\rm W}} = \frac{-e}{1 + \frac{C_{\rm W}}{C_{\rm G}} + \frac{C_{\rm Q}(\delta)}{C_{\rm G}}} \approx \frac{-e}{1 + \frac{C_{\rm W}}{C_{\rm G}}} \tag{5}$$

 $C_{\mathbb{Q}}$ (δ) is the quantum capacitance of the semiconductor described by

$$C_{\mathcal{Q}}(\delta) = e^{\frac{d\mathcal{Q}(\delta)}{d\delta}} \tag{6}$$

 $C_{\rm Q}$ (δ) represents the density of states of the ZnO electrode (in the unit of capacitance). Assuming there are no in-gap trap states in ZnO, $C_{\rm Q}$ (δ) is negligible because $E_{\rm F}$ lies within the bandgap. Accordingly, $\Delta\delta$ is estimated to be as large as 1.2 eV when varying $V_{\rm G}$ between -2 and +8 V. This is a very large value, and it is made possible by the exceptional gate capacitance $C_{\rm G}$ that we obtained using a thin HfO₂ dielectric.

Correspondingly, when a reduction reaction occurs, electrons in the semiconductor conduction band transfer into the empty states of the redox acceptor in an electron tunneling process. The charge transfer rate is proportional to the overlap between the filled electrode states and empty redox states. The position and distribution of the redox density of states (DOS) are determined by the formal potential (U^0) and solvent reorganization energy (λ) of the redox couple.²⁹ At $V_{\rm G}=0$ V, the charge transfer rate is relatively weak because of poor overlap of the occupied ZnO conduction band states with the empty redox states. However, as the conduction band edge is lowered when applying a positive $V_{\rm G}$, the energy state overlap increases, and heterogeneous charge transfer is thus enhanced. This occurs for both the TCNQ and TBBQ cases. If much higher V_G is applied, the conduction band edge can be pushed far lower and it is possible that the charge transfer rate then decreases again because of poor overlap, as shown in Figure 5b.

Our interpretation is thus that in the case of TCNQ reduction, because eU^0 lies deeper in the bandgap, we are not able to push the conduction band edge down sufficiently to see $k_{\rm ET}$ increase, peak, and then decrease. That is, we probe only the upper side of the redox DOS. For TBBQ on the other hand, whose eU^0 is closer to the ZnO conduction band edge, we propose that the conduction band edge is tuned through the TBBQ density of states and that the $k_{\rm ET}$ vs $V_{\rm G}$ behavior essentially represents a convolution of the filled electrode states with the envelope of empty redox states in solution. This has been made possible by the action of the back gate potential.

CONCLUSION

In summary, we have achieved a substantial modulation of electrochemical charge transfer rates at ultrathin ZnO electrodes by applying independent back gate biases, $V_{\rm G} \leq 8$ V. The key innovation here was incorporation of a high-k gate dielectric into the MIS working electrode stack, which lowered the gate voltages and simultaneously increased gating effectiveness as quantified by the ability to modulate $k_{\rm ET}$ by up to a factor of 30. The mechanism of gate enhancement is the transverse field effect, whereby the electric field produced

by the back gate perpendicular to the semiconductor layer pulls down the conduction and valence band edges in the semiconductor, simultaneously allowing the layer to be flooded with electrons. Both the band edge shift and the increased carrier density are essential to changing the overall interfacial charge transfer rate $(I_{\rm W})$, but $k_{\rm ET}$ specifically reflects the semiconductor band edge realignment. Simultaneously in this work we have demonstrated the essentially ideal behavior of the double layer and back gate capacitors; both are well-coupled in series to the ZnO layer and both modulate charge and band alignment with the redox couple. In future studies we will apply the working electrode MIS stack described here to control rates of electrocatalytic reactions.

ASSOCIATED CONTENT

Supporting Information

The Supporting Information is available free of charge at https://pubs.acs.org/doi/10.1021/acsami.2c18549.

Discussions of materials, electronic measurement, and voltammogram of redox couples on Au electrode and figures of AFM, XPS and XRD spectra of ZnO film, thickness measurement of HfO₂ and Pd, device fabrication procedure, optical image of the ZnO FET device with the PDMS microfluidic channel, capacitor current measurement on the ZnO/HfO₂/Pd stack, cyclic voltammogram of TCNQ and TBBQ on Au electrode, forward and reverse sweeps of the steady state voltammogram on Au and ZnO electrode, and redox chemistry in ionic liquid (EMI-TFSI) (PDF)

AUTHOR INFORMATION

Corresponding Author

C. Daniel Frisbie — Department of Chemistry, University of Minnesota, Minneapolis, Minnesota 55455, United States; Department of Chemical Engineering and Materials Science, University of Minnesota, Minneapolis, Minnesota 55455, United States; orcid.org/0000-0002-4735-2228; Email: frisbie@umn.edu

Authors

Yuxin Wang — Department of Chemistry, University of Minnesota, Minneapolis, Minnesota 55455, United States; orcid.org/0000-0002-6590-6087

Yan Wang — Department of Chemistry, University of Minnesota, Minneapolis, Minnesota 55455, United States; orcid.org/0000-0003-1264-3794

Complete contact information is available at: https://pubs.acs.org/10.1021/acsami.2c18549

Notes

The authors declare no competing financial interest.

ACKNOWLEDGMENTS

This work was primarily supported by the Department of Energy, Basic Energy Sciences Catalysis Program (DE-SC0021163). Parts of the work were carried out in the Characterization Facility at University of Minnesota, which is partially supported by the NSF through the MRSEC program (DMR-2011401). Other portions of this work were conducted in the Minnesota Nano Center, which is supported by the NSF through the National Nano Coordinated Infra-structure Network (NNCI) under Award Number ECCS-2025124.

The authors thank Jiazhen Xu for help with AFM measurements.

REFERENCES

- (1) Kim, C. H.; Frisbie, C. D. Field Effect Modulation of Outer-Sphere Electrochemistry at Back-Gated, Ultrathin ZnO Electrodes. *J. Am. Chem. Soc.* **2016**, *138* (23), 7220–3.
- (2) Wang, Y.; Kim, C.-H.; Yoo, Y.; Johns, J. E.; Frisbie, C. D. Field Effect Modulation of Heterogeneous Charge Transfer Kinetics at Back-Gated Two-Dimensional MoS₂ Electrodes. *Nano Lett.* **2017**, *17* (12), 7586–7592.
- (3) Yang, H.; He, Q.; Liu, Y.; Li, H.; Zhang, H.; Zhai, T. On-Chip Electrocatalytic Microdevice: An Emerging Platform for Expanding the Insight into Electrochemical Processes. *Chem. Soc. Rev.* **2020**, 49 (10), 2916–2936.
- (4) Kim, C. H.; Wang, Y.; Frisbie, C. D. Continuous and Reversible Tuning of Electrochemical Reaction Kinetics on Back-Gated 2D Semiconductor Electrodes: Steady-State Analysis Using a Hydrodynamic Method. *Anal. Chem.* **2019**, *91* (2), 1627–1635.
- (5) Kim, C.-H.; Frisbie, C. D. Determination of Quantum Capacitance and Band Filling Potential in Graphene Transistors with Dual Electrochemical and Field-Effect Gates. *J. Phys. Chem. C* **2014**, *118* (36), 21160–21169.
- (6) Ding, M.; He, Q.; Wang, G.; Cheng, H.-C.; Huang, Y.; Duan, X. An On-Chip Electrical Transport Spectroscopy Approach for in situ Monitoring Electrochemical Interfaces. *Nat. Commun.* **2015**, *6* (1), 1–9.
- (7) Wang, Y.; Udyavara, S.; Neurock, M.; Frisbie, C. D. Field Effect Modulation of Electrocatalytic Hydrogen Evolution at Back-Gated Two-Dimensional MoS₂ Electrodes. *Nano Lett.* **2019**, *19* (9), 6118–6123.
- (8) Wang, J.; Yan, M.; Zhao, K.; Liao, X.; Wang, P.; Pan, X.; Yang, W.; Mai, L. Field Effect Enhanced Hydrogen Evolution Reaction of MoS₂ Nanosheets. *Adv. Mater.* **2017**, *29* (7), 1604464.
- (9) Yan, M.; Pan, X.; Wang, P.; Chen, F.; He, L.; Jiang, G.; Wang, J.; Liu, J. Z.; Xu, X.; Liao, X.; Yang, J.; Mai, L. Field-Effect Tuned Adsorption Dynamics of VSe₂ Nanosheets for Enhanced Hydrogen Evolution Reaction. *Nano Lett.* **2017**, *17* (7), 4109–4115.
- (10) Pan, Y.; Wang, X.; Zhang, W.; Tang, L.; Mu, Z.; Liu, C.; Tian, B.; Fei, M.; Sun, Y.; Su, H.; Gao, L.; Wang, P.; Duan, X.; Ma, J.; Ding, M. Boosting the Performance of Single-Atom Catalysts via External Electric Field Polarization. *Nat. Commun.* **2022**, *13* (1), 3063.
- (11) Waelder, J.; Vasquez, R.; Liu, Y.; Maldonado, S. A Description of the Faradaic Current in Cyclic Voltammetry of Adsorbed Redox Species on Semiconductor Electrodes. *J. Am. Chem. Soc.* **2022**, *144* (14), 6410–6419.
- (12) Voiry, D.; Fullon, R.; Yang, J.; de Carvalho Castro e Silva, C.; Kappera, R.; Bozkurt, I.; Kaplan, D.; Lagos, M. J.; Batson, P. E.; Gupta, G.; et al. The Role of Electronic Coupling Between Substrate and 2D MoS₂ Nanosheets in Electrocatalytic Production of Hydrogen. *Nat. Mater.* **2016**, *15* (9), 1003–1009.
- (13) He, Y.; He, Q.; Wang, L.; Zhu, C.; Golani, P.; Handoko, A. D.; Yu, X.; Gao, C.; Ding, M.; Wang, X. Self-Gating in Semiconductor Electrocatalysis. *Nat. Mater.* **2019**, *18* (10), 1098–1104.
- (14) Yan, M.; Pan, X.; Wang, P.; Chen, F.; He, L.; Jiang, G.; Wang, J.; Liu, J. Z.; Xu, X.; Liao, X.; et al. Field-Effect tuned adsorption dynamics of VSe₂ nanosheets for enhanced hydrogen evolution reaction. *Nano Lett.* **2017**, *17* (7), 4109–4115.
- (15) Ding, M.; Zhong, G.; Zhao, Z.; Huang, Z.; Li, M.; Shiu, H.-Y.; Liu, Y.; Shakir, I.; Huang, Y.; Duan, X. On-Chip in situ Monitoring of Competitive Interfacial Anionic Chemisorption as a Descriptor for Oxygen Reduction Kinetics. *ACS Cent. Sci.* **2018**, *4* (5), 590–599.
- (16) Wu, Y.; Ringe, S.; Wu, C. L.; Chen, W.; Yang, A.; Chen, H.; Tang, M.; Zhou, G.; Hwang, H. Y.; Chan, K.; Cui, Y. A Two-Dimensional MoS₂ Catalysis Transistor by Solid-State Ion Gating Manipulation and Adjustment (SIGMA). *Nano Lett.* **2019**, *19* (10), 7293–7300.
- (17) Cao, D.; Wang, Z.; Wen, L.; Mi, Y.; Lei, Y. Switchable Charge-Transfer in the Photoelectrochemical Energy-Conversion Process of

- Ferroelectric BiFeO₃ Photoelectrodes. *Angew. Chem.* **2014**, 126 (41), 11207–11211.
- (18) Singh, S.; Sangle, A. L.; Wu, T.; Khare, N.; MacManus Driscoll, J. L. Growth of doped SrTiO₃ ferroelectric nanoporous thin films and tuning of photoelectrochemical properties with switchable ferroelectric polarization. *ACS Appl. Mater. Interfaces* **2019**, *11* (49), 45683–45691.
- (19) Huang, A. P.; Yang, Z.; Chu, P. K. Advances in Solid State Circuits Technologies; Intech, 2010; pp 333-350.
- (20) Shim, J. H.; Choi, H. J.; Kim, Y.; Torgersen, J.; An, J.; Lee, M. H.; Prinz, F. B. Process-Property Relationship in High-k ALD SrTiO₃ and BaTiO₃: A Review. *J. Mater. Chem. C* **2017**, *5* (32), 8000–8013.
- (21) Fischer, D.; Kersch, A. The Effect of Dopants on the Dielectric Constant of HfO₂ and ZrO₂ from First Principles. *Appl. Phys. Lett.* **2008**, 92 (1), 012908.
- (22) Ortiz, R. P.; Facchetti, A.; Marks, T. J. High-k Organic, Inorganic, and Hybrid Dielectrics for Low-Voltage Organic Field-Effect Transistors. *Chem. Rev.* **2010**, *110* (1), 205–239.
- (23) Gu, D.; Dey, S. K.; Majhi, P. Effective Work Function of Pt, Pd, and Re on Atomic Layer Deposited HfO₂. *Appl. Phys. Lett.* **2006**, 89 (8), 082907.
- (24) Pandey, S. K.; Pandey, S. K.; Mukherjee, C.; Mishra, P.; Gupta, M.; Barman, S. R.; D'Souza, S. W.; Mukherjee, S. Effect of growth temperature on structural, electrical and optical properties of dual ion beam sputtered ZnO thin films. *J. Mater. Sci. Mater. Electron.* **2013**, 24 (7), 2541–2547.
- (25) Torchynska, T.; Vega Macotela, L. G.; Khomenkova, L.; Gourbilleau, F.; Lartundo Rojas, L. Annealing impact on emission and phase varying of Nd-doped Si-rich-HfO₂ films prepared by RF magnetron sputtering. *J. Mater. Sci. Mater. Electron.* **2020**, *31* (6), 4587–4594.
- (26) Neamen, D. Semiconductor Physics and Devices: Basic Principles; Mc Graw Hill: New York, 2012; pp 371–490.
- (27) Xie, W.; Frisbie, C. D. Organic Electrical Double Layer Transistors Based on Rubrene Single Crystals: Examining Transport at High Surface Charge Densities above 10¹³ cm⁻². *J. Phys. Chem. C* **2011**, *115* (29), 14360–14368.
- (28) Liang, Y.; Chang, H. C.; Ruden, P. P.; Frisbie, C. D. Examination of Au, Cu, and Al Contacts in Organic Field-Effect Transistors via Displacement Current Measurements. *J. Appl. Phys.* **2011**, *110* (6), 064514.
- (29) Nozik, A. J.; Memming, R. Physical Chemistry of Semiconductor-Liquid Interfaces. *J. Phys. Chem.* **1996**, *100* (31), 13061–13078.
- (30) Morrison, S. R.; Morrison, S. Electrochemistry at Semiconductor and Oxidized Metal Electrodes; Springer: New York, 1980; Vol. 126, pp 84–95.
- (31) Heffner, J. E.; Wigal, C. T.; Moe, O. A. Solvent Dependence of the One-Electron Reduction of Substituted Benzo- and Naphthoquinones. *Electroanalysis* **1997**, *9* (8), 629–632.
- (32) Kohl, P.; Bard, A. Semiconductor Electrodes. 13. Characterization and Behavior of n-Type Zinc Oxide, Cadmium Sulfide, and Gallium Phosphide Electrodes in Acetonitrile Solutions. *J. Am. Chem. Soc.* 1977, 99 (23), 7531–7539.
- (33) Bano, K.; Nafady, A.; Zhang, J.; Bond, A. M.; Inam ul, H. Electrode Kinetics Associated with Tetracyanoquinodimethane (TCNQ), TCNQ¹, and TCNQ² Redox Chemistry in Acetonitrile as Determined by Analysis of Higher Harmonic Components Derived from Fourier Transformed Large Amplitude ac Voltammetry. *J. Phys. Chem. C* 2011, 115 (49), 24153–24163.
- (34) Rees, N. V.; Clegg, A. D.; Klymenko, O. V.; Coles, B. A.; Compton, R. G. Marcus Theory for Outer-Sphere Heterogeneous Electron Transfer: Predicting Electron-transfer Rates for Quinones. *J. Phys. Chem. B* **2004**, *108* (34), 13047–13051.
- (35) Li, W.; Tan, C.; Lowe, M. A.; Abruña, H. D.; Ralph, D. C. Electrochemistry of Individual Monolayer Graphene Sheets. *ACS Nano* **2011**, *5* (3), 2264–2270.
- (36) Rees, N. V.; Klymenko, O. V.; Coles, B. A.; Compton, R. G. The High Speed Channel Electrode Applied to Heterogeneous

- Kinetics: the Oxidation of 1, 4-phenylenediamines and Related Species in Acetonitrile. *J. Electroanal. Chem.* **2002**, 534 (2), 151–161.
- (37) Rees, N. V.; Dryfe, R. A.; Cooper, J. A.; Coles, B. A.; Compton, R. G.; Davies, S. G.; McCarthy, T. D. Voltammetry under High Mass Transport Conditions. A High Speed Channel Electrode for the Study of Ultrafast Kinetics. *J. Phys. Chem.* **1995**, *99* (18), 7096–7101.
- (38) Bard, A. J. Photoelectrochemistry. Science 1980, 207 (4427), 139-144.
- (39) Foley, J. M.; Price, M. J.; Feldblyum, J. I.; Maldonado, S. Analysis of the Operation of Thin Nanowire Photoelectrodes for Solar Energy Conversion. *Energy Environ. Sci.* **2012**, 5 (1), 5203–5220.
- (40) Faulkner, L. R.; Bard, A. J. Electrochemical Methods: Fundamentals and Applications; John Wiley and Sons, 2002; pp 337–344.
- (41) Gerischer, H. Physical Chemistry: An Advanced Treatise; Elsevier, 1970; pp 487–489.
- (42) Clegg, A. D.; Rees, N. V.; Klymenko, O. V.; Coles, B. A.; Compton, R. G. Marcus Theory of Outer-Sphere Heterogeneous Electron Transfer Reactions: Dependence of the Standard Electrochemical Rate Constant on the Hydrodynamic Radius from High Precision Measurements of the Oxidation of Anthracene and Its Derivatives in Nonaqueous Solvents Using the High-Speed Channel Electrode. J. Am. Chem. Soc. 2004, 126 (19), 6185–6192.

□ Recommended by ACS

The Role of Electrostatic Binding Interfaces in the Performance of Bacterial Reaction Center Biophotoelectrodes

Milo R. van Moort, Vincent M. Friebe, et al.

FEBRUARY 07, 2023

ACS SUSTAINABLE CHEMISTRY & ENGINEERING

DEAD E

Enhancing Protein Adsorption for Improved Lateral Flow Assay on Cellulose Paper by Depleting Inert Additive Films Using Reactive Plasma

Yi Zhang, Jackie Y. Ying, et al.

JANUARY 24, 2023

ACS APPLIED MATERIALS & INTERFACES

READ 🗹

$\label{eq:molecular and Atomic Layer Deposition of Hybrid} Polyimide-Al_2O_3\ Gate\ Dielectrics\ for\ Flexible\ Electronic\ Devices$

Jialiang Wang, Xinwei Wang, et al.

OCTOBER 05, 2022

CHEMISTRY OF MATERIALS

READ 🗹

Redox Polyelectrolytes with pH-Sensitive Electroactive Functionality in Aqueous Media

Kai-Jher Tan, T. Alan Hatton, et al.

FEBRUARY 16, 2023

LANGMUIR

READ 🗹

Get More Suggestions >